Characterization of Plasma Etching Process Damage in HgCdTe

A. GAUCHER,[1,3] J. BAYLET,[1] J. ROTHMAN,[1] E. MARTINEZ,[1]
and C. CARDINAUD[2]

1.—CEA-LETI, Minatec Campus, 17 rue des Martyrs, 38054 Grenoble Cedex 9, France.
2.—Institut des Matériaux Jean Rouxel (IMN), Université de Nantes, CNRS, 2 rue de la Houssinière, BP 32229, 44322 Nantes Cedex 3, France. 3.—e-mail: alexandre.gaucher@cea.fr

Microstructural and electrical damage to n-type long-wavelength infrared $Hg_{1-x}Cd_xTe$ (MCT) following CH_4-H_2-based inductively coupled plasma etching has been investigated. While the damage from such etching processes to MCT has previously been characterized for planar full-wafer etching, in this communication we present the results of an investigation of the damage incurred to etched sidewalls, whose faces constitute the majority of the etched surface in novel architectures. Auger electron spectroscopy was used to monitor the evolution of X_{Cd} beneath etched surfaces. So far, no X_{Cd} evolution has been detected underneath etched surfaces within a $\Delta X_{Cd} = 0.02$ resolution. Conductivity and minority-carrier lifetime have been studied on patterned photoconductors, from which it is possible to extract a surface recombination velocity (SRV). These studies have shown surface conductivity variations and SRV shifts of several orders of magnitude, depending on the etching process used.

Key words: HgCdTe, inductively coupled plasma (ICP), etched sidewalls, Auger electron spectroscopy, minority-carrier lifetime

INTRODUCTION

Since its first synthesis in the early 1960s, HgCdTe has proved itself to be the most suitable material for a wide range of infrared detection applications.[1] Increasing device complexity has brought numerous material processing challenges that must be addressed in order to fabricate the latest generation of infrared detectors; for example, many advanced pixel architectures include high-aspect-ratio trenches.[2] Over the decades, different etching processes have been developed to pattern HgCdTe.[3] Wet etching was commonly used until the reduction in pixel pitch and a growing need for anisotropic profiles necessitated dry etching processes such as ion beam etching (IBE) and plasma etching. However, due to the ternary nature of HgCdTe and the presence of Hg in the lattice, many of these etching techniques lead to microstructural surface damage and the deterioration of electrical properties.

The most widely studied etch-induced surface effect is so-called p-to-n conversion. It has been shown that IBE[4,5] and plasma etching[6] of p-type materials leads to an inversion of the doping type. This phenomenon has attracted much interest, as both IBE[7,8] and plasma etching[9,10] have proven to be suitable methods for the formation of controlled junctions in the fabrication of photodiodes. However, dry etching is also used in other process steps in which the modification of surface properties is not desired. In such cases it is important to precisely understand the impact of the etching step on the material. The effects of IBE,[11,12] wet etching,[11,13–17] and plasma etching[18,19] on planar surfaces have been investigated over the years using both electrical and material characterization techniques. X-ray photoelectron spectroscopy has been the most widely used material characterization technique for full-wafer etching studies;[11–13,17–19] however, several other techniques such as Auger electron

spectroscopy (AES),[12] secondary-ion mass spectrometry (SIMS),[12] atomic force microscopy,[17,18] x-ray diffraction[16] or reflection high-energy electron diffraction[18] have also been employed. Electrical characterization such as minority-carrier lifetime,[14,15,17] noise,[14] and capacitance–voltage measurements[15,16] have also been reported.

Plasma etching is becoming the etching process of choice to structure HgCdTe as it potentially combines the smooth and damage-free mechanism of wet etching with the desirable anisotropy properties of dry etching. Several authors have studied the influence of plasma etching on multispectral mesa-based devices. However, these works concerned only detectors and/or photodiodes where the responsivity,[20] specific detectivity,[20] laser beam-induced current,[20] photodiode noise,[20,21] and current–voltage curves[22] were used to indirectly probe the etching-related effects.

In this work, we present both material and electrical characterization of mesa structures. The spatial resolution of AES has been exploited to investigate the potential stoichiometric evolution occurring beneath the etched sidewalls of trench-etched samples. Measurements of conductivity and minority-carrier lifetime have been performed on sidewall dedicated test structures to understand the interaction between charge carriers and etched materials. Different etching processes such as IBE, plasma etching, and hybrid plasma + wet etching have been investigated. After a presentation of the samples used in this study and the various microstructural and electrical characterization techniques, we focus on the results obtained using each technique in order to gain an insight into the etching-related effects.

EXPERIMENTAL PROCEDURES

Samples

Various samples were analyzed using AES. Two reference samples were used to check the quantification of the surface chemical composition: these consisted of stacks of HgCdTe layers with variable Cd composition grown by molecular beam epitaxy on (211)-oriented CdZnTe. Several trench-etched samples of long-wavelength infrared (LWIR) HgCdTe were also grown by liquid-phase epitaxy on (111)-oriented CdZnTe. These samples were then subjected to IBE or plasma etching.

The starting material used for electrical characterization was n-type LWIR HgCdTe grown by liquid-phase epitaxy on (111)-oriented CdZnTe. n-Type doping was achieved using indium at $\sim 10^{15}$ cm^{-3}. Fourier-transform infrared (FTIR) spectroscopy was performed on each sample prior to the etching process, which gave the cut-off wavelength as well as the thickness of the sample. Mesas were defined by etching down to the substrate using a standard photolithography process. These structures were then treated using standard HgCdTe surface passivation techniques, and metallic contacts were deposited onto contact areas. Figure 1a presents a schematic diagram of a photoconductor designed to study minority-carrier lifetime. Structures with a range of widths from 8 μm to 90 μm were produced (Fig. 1b). As etching can reduce the width of the photoconductors, this dimension was optically measured after processing. The samples used are listed with their thickness and cut-off wavelength in Table I. Three different etching types were used: plasma etching of samples 1 and 2 used a CH$_4$-H$_2$-based chemistry in an inductively coupled plasma device already described elsewhere;[19] sample 3 was etched by combining the previously described plasma etching and a light wet etch to remove the plasma-induced surface damage; IBE of sample 4 used a standard Ar$^+$ beam used in different photodiode processes at LETI. Of all the samples tested, only sample 1 did not undergo any post-etch "healing" process. This sample also originated from a separate epitaxial growth to that of samples 2, 3, and 4.

Microstructural Characterization

AES line scans were acquired with a PHI 700Xi scanning Auger nanoprobe equipped with a
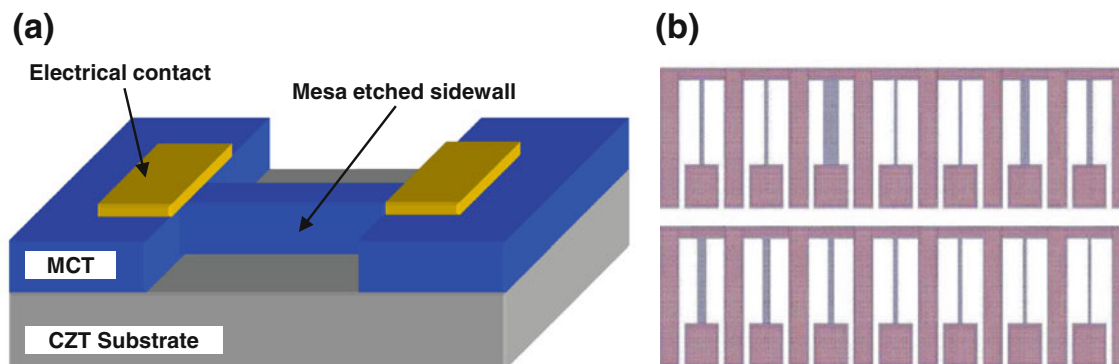

Fig. 1. (a) Schematic diagram of a sidewall dedicated patterned photoconductor. (b) Variable width photoconductors.

Table I. Sample list

Sample	MCT Thickness (μm)	Cut-Off Wavelength at 300 K (μm)	Etching Type	Healing Process?
1	5.2	6.30	Plasma	No
2	5	6.32	Plasma	Yes
3	5	6.32	Plasma + wet	Yes
4	5	6.32	IBE	Yes

cylindrical mirror analyzer and a coaxial electron gun. A sputter ion gun was used to control the surface state prior to AES analysis. The ion beam consisted of Ar^+ ions with an acceleration voltage of 1 keV and an incidence angle of 72° from the sample normal. A 10-keV 10-nA primary electron beam was used for the AES measurements. Cd (MNN) and Te (MNN) spectra were acquired in the direct mode, then a numerical nine-point Savitzky–Golay smoothing and differentiation filter was applied.

As is known from the literature regarding HgCdTe, Hg loss can occur during analysis due to local heating caused by the electron beam.[12,23–25] To prevent this effect, different solutions have been reported, e.g., the use of a cryogenic sample holder[24,25] or precise monitoring of the measurement parameters to ensure the reproducibility of experimental conditions.[23] The latter methodology has been adopted at LETI, and every AES result presented here was acquired using this method.

Electrical Characterization

Photoconductive decay (PCD) measurements were performed in a Janis ST500 cryostat at 77 K. Constant voltage was applied through a bias tee using a Keithley 236 generator while optical excitation was delivered via an optical fiber from a Calmar Optcom GSL-01TFCEA11 laser source at wavelength of 1.55 μm. The laser source was modulated with a Stanford DG535 pulse generator that also trigged a LeCroy WavePro 725Zi oscilloscope. Changes in conductance were measured using a Femto DUPVA-1-70 preamplifier to detect transient voltages and then recorded by the oscilloscope. To avoid problems arising from different signal intensities, recorded decays were normalized (Fig. 2). Several experimental parameters were checked to avoid misleading effects: the optical fiber position and the bias were chosen to avoid carrier sweep-out effects through the contacts, and the optical injection power was monitored to ensure a low carrier injection level.

Conductivity stemmed from simple current–voltage measurements at 77 K on the patterned photoconductors. From the known photoconductor geometry, the conductivity was then derived. The length of the photoconductors used in the calculation was the mask value, whereas the width and the thickness were measured optically and extracted from FTIR results, respectively.
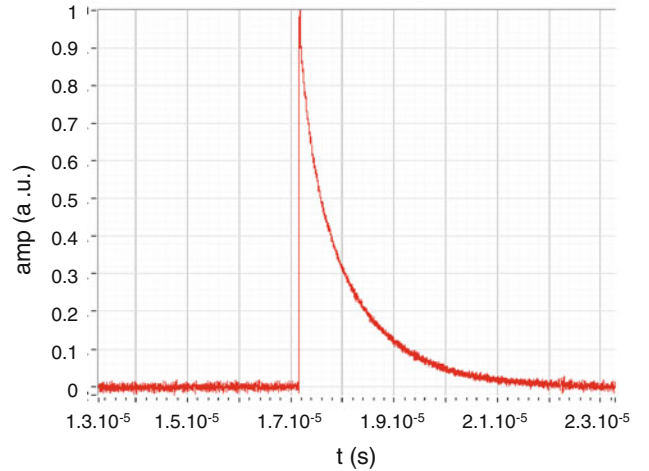

Fig. 2. Normalized PCD decay.

RESULTS AND DISCUSSION

Auger Electron Spectroscopy

AES has been developed to address the problem of stoichiometric modifications of etched sidewalls. So far, quantification has been achieved in the range $0.2 < X_{Cd} < 0.3$. Figure 3a shows an Auger line scan of the cross-section of a HgCdTe stack of variable Cd composition. The minimum X_{Cd} variation of this stack is $\Delta X_{Cd} = 0.07$. Also displayed are the expected composition and a SIMS profile of the stack. On this sample, the AES quantification is accurate for X_{Cd} values lying in the range $0.2 < X_{Cd} < 0.3$, while being less precise for higher X_{Cd} values. The SIMS profile allows a comparison of the precision of the AES analysis with another routinely used material characterization method. For low X_{Cd} values, SIMS correctly matches the expected composition even if it seems to be slightly less accurate than AES. However, SIMS data show less fluctuation than the AES data. For higher X_{Cd} values, both methods lose precision. The reduced range of the SIMS profile compared with the expected composition is believed to be due to an incorrect calibration of the SIMS sputtering velocity. Figure 3b presents an Auger line scan of the cross-section of a second HgCdTe stack of variable Cd composition. This time, the minimum X_{Cd} variation is $\Delta X_{Cd} = 0.02$, which is correctly discriminated by the AES analysis. Quantification is accurate for X_{Cd} values lying in the range
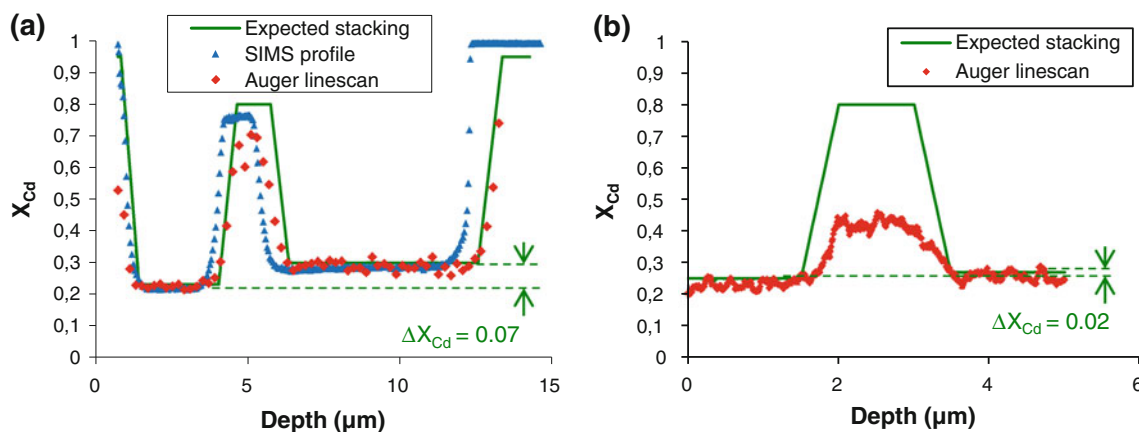
(a)

(b)

Fig. 3. Auger line scans of the cross-section of two HgCdTe stacks made up of layers of variable Cd composition.

$0.2 < X_{Cd} < 0.3$ but again is less precise for higher X_{Cd} values.

Controlled and constant measurement conditions and quantification routine were used on trench-etched samples, realized using standard multispectral plasma etching and standard IBE. Figure 4 presents an Auger line scan of the cross-section of a plasma-etched trench in which no X_{Cd} evolution can be detected beneath the etched sidewall surface. The potential change in composition induced by plasma etching is therefore smaller than the detection limit of $\Delta X_{Cd} = 0.02$. The same observation has been made on an equivalent IBE-etched sample.

Whereas material characterization directly measures etching-induced stoichiometric evolution, etching-related effects may also be indirectly determined by studying the charge carrier behavior in proximity to an etched surface. For this purpose, conductivity and minority-carrier lifetime measurements are presented here.

Conductivity Measurements

We developed a sidewall damage model (Fig. 5) that supposes a damaged depth δw and a surface conductivity σ_s on each etched face of the photoconductor. The total conductance of the photoconductor is the sum of the bulk and the surface contributions. One can therefore link the measured conductivity to the photoconductor width:

$$\sigma = \sigma_b + 2(\sigma_s - \sigma_b)\delta w \frac{1}{w},$$

where σ_b is the bulk conductivity and w is the photoconductor width. By applying this model to a set of measured conductivities, it is possible to extract information regarding the damaged surfaces. Obviously, both δw and σ_s are not available from a single fit.

Figure 6a shows the measured conductivity as a function of the inverse photoconductor width for sample 1. A linear decrease of the conductivity is observed. The negative slope of the fitted model
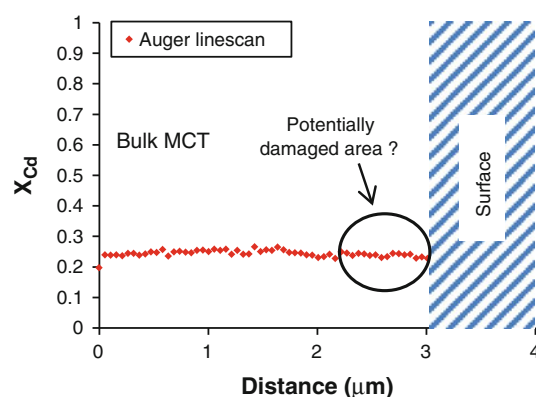

Fig. 4. Auger line scan of the cross-section of a plasma-etched trench.
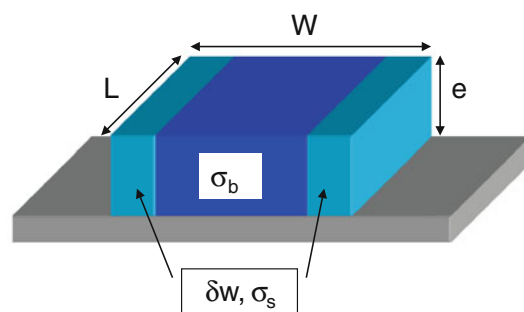

Fig. 5. Schematic diagram of a photoconductor with damaged sidewalls.

implies $\sigma_s < \sigma_b$, which means that the etched faces of the photoconductor present either carrier depletion or reduced mobility. Figure 6b presents an equivalent plot for sample 2. The tendency is the opposite; the positive slope of the fit indicates that $\sigma_s > \sigma_b$, which means that the photoconductor faces show either carrier accumulation or enhanced mobility (very unlikely). Samples 3 and 4 exhibit a similar tendency to that of sample 2. Quantitative comparison of the samples is possible through the extracted gradients, although these gradient values are not
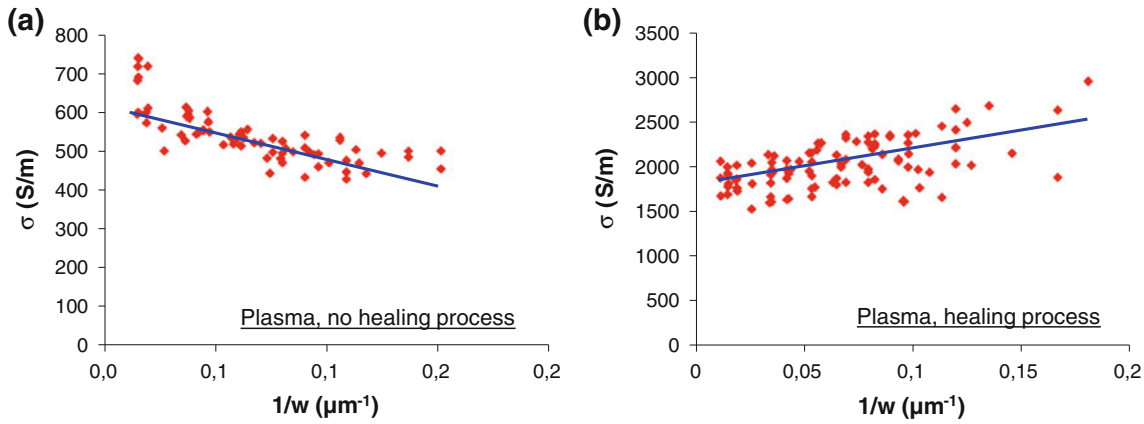
Fig. 6. Measured conductivity as a function of inverse photoconductor width for (a) sample 1 and (b) sample 2.

Table II. Extracted surfaces conductivities of samples 2, 3, and 4 for a supposed damaged depth of 500 nm

Sample	σ_s/σ_b
2: Plasma, healing process	6.8
3: Plasma + wet, healing process	1.7
4: IBE, healing process	3.3

directly representative of physical quantities. At this point, for the sake of simplicity, we assume a value for the damaged depth in order to compare samples 2, 3, and 4. Estimating a damaged depth of 500 nm for samples 2, 3, and 4 allows the extraction of a surface conductivity value for each sample. Although it is highly probable that the damaged depth is different for each sample, and is not necessarily around 500 nm, this exercise serves to illustrate the differences between the three samples. The results are presented in Table II. The extracted surface conductivities are given relative to the bulk conductivities in order to compensate for the bulk variations between the samples. The ratio of the surface conductivity to the bulk conductivity is greatly reduced

by the light wet etching step after plasma etching, reducing the extra conductivity from seven times the bulk conductivity (sample 2) to around twice the bulk conductivity (sample 3). This confirms that the wet etching step effectively reduces the surface damage (i.e., the conductivity changes) induced by plasma etching on the etched sidewalls. From these results, one can also say that IBE seems to affect the conductivity to a lesser degree than plasma etching.

The conductivity results are necessary in order to interpret the carrier lifetime results. Sample 1 exhibits carrier depletion and/or reduced mobility on the photoconductor faces, while samples 2, 3, and 4 exhibit carrier accumulation. Using a simple band diagram, one can understand that minority carriers will preferentially interact with depleted surfaces (Fig. 7a) rather than with accumulated surfaces (Fig. 7b).

Minority-Carrier Lifetime

The minority-carrier lifetime of a photoconductor is determined by various recombination mechanisms: bulk recombinations, top and back surface recombinations, and sidewall recombinations. The lifetime resulting from bulk and top and back sur-
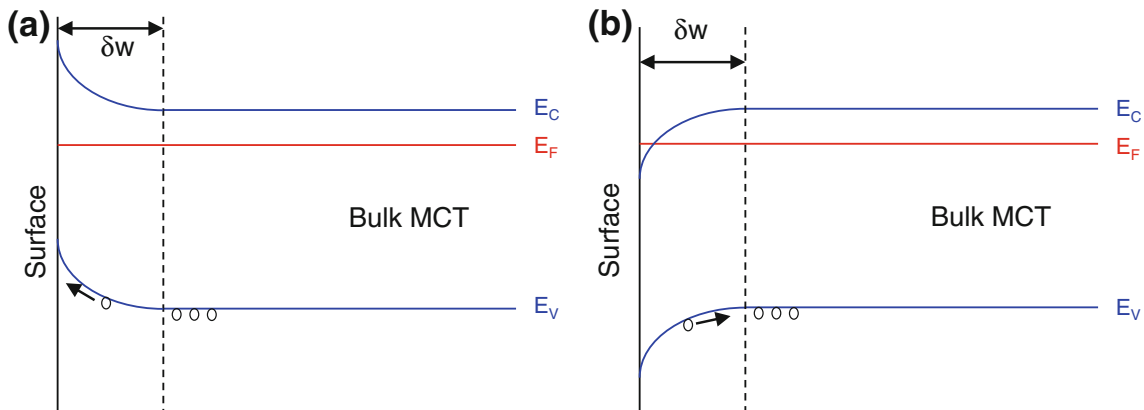

Fig. 7. Band diagram of (a) a depleted surface and (b) an accumulated surface.

face contributions was measured on specific planar PCD structures (Fig. 8). In this paper, the "measured bulk lifetime" includes bulk recombinations as well as top and back surface contributions, whereas the "real bulk lifetime" refers to bulk recombinations only. The measured bulk lifetime may be lower than the real bulk lifetime. The order of magnitude of the measured bulk lifetimes is 1 μs, which is in accordance with the theoretically
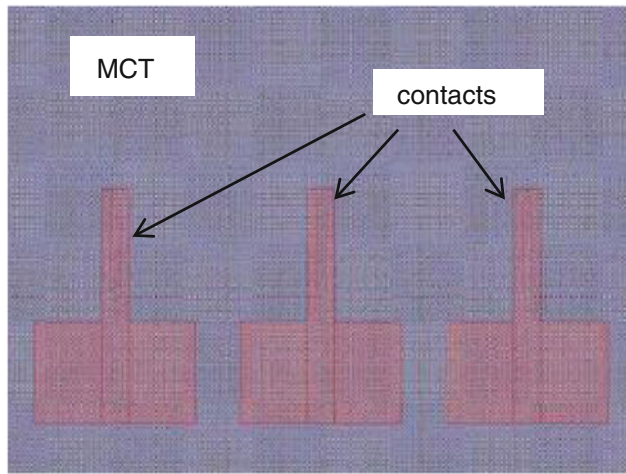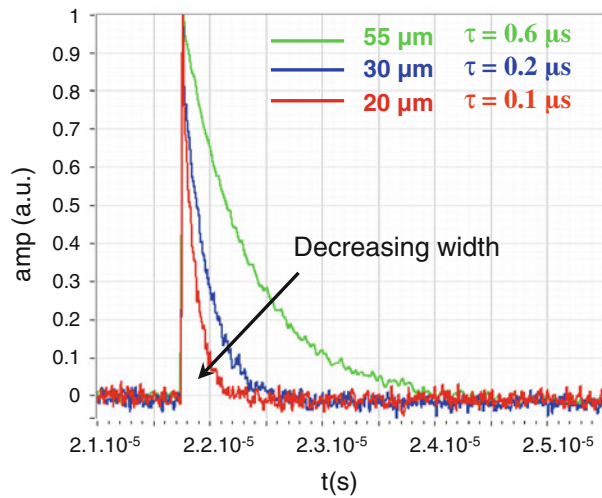

Fig. 8. Bulk lifetime test structure.

Fig. 9. Lifetime evolution versus photoconductor width.

calculated lifetimes.[26] Measured bulk lifetimes may vary between samples for various reasons; for example, there may be variations of the doping level within a same epitaxy. As the lifetime evolves proportionally to $1/N_{dop}^2$, where N_{dop} is the doping level, a small doping variation can lead to a substantial change in carrier lifetime. Furthermore, the passivation layer may present slight differences between samples, which would lead to a varying surface recombination strength. Also, the possibility of local defects affecting the planar structures dedicated to bulk lifetime measurements cannot be excluded.

A typical dependence of the measured carrier lifetime on the photoconductor width is shown in Fig. 9, in which the lifetime decreases with the width. This behavior can be explained by considering that the sidewalls constitute a greater proportion of the surface for narrower photoconductors, leading to a greater contribution from sidewall recombinations. To quantify this tendency, we use a phenomenological model:

$$\frac{1}{\tau} = \frac{1}{\tau_{bulk}} + \alpha \frac{S}{w},$$

where τ is the measured lifetime, τ_{bulk} is the bulk lifetime, S is the surface recombination velocity (SRV) that is indicative of the sidewall recombination rate, and α is a fitting parameter. The experimental system was simulated using Silvaco software. The model was fitted to the resulting numerical data, giving the fitting parameter α. Of course, the value of α is only valid for a particular set of parameters, such as the bulk minority-carrier mobility and the material doping level (we use an α value of 0.0116 in this study). The resulting SRV value may not be the absolute value, but both the order of magnitude and, more importantly, the relative change in SRV between each sample can be assumed to be correct, as the carrier mobility is not expected to vary between samples. The extracted SRV is an effective SRV and represents the combined effects of the actual SRV, which results from minority-carrier recombination on the sidewalls, and of the ability of the minority carriers to effectively reach the sidewall. The latter mechanism is related to the conductivity results. An accumulated surface observed for samples 2, 3, and 4 (Table II) acts like a shielding of the sidewall (Fig. 7b).

Table III. Minority-carrier lifetime measurement results

Sample	Measured τ_{bulk} (μs)	Extracted τ_{bulk} (μs)	Extracted S (cm/s)
1: Plasma, no healing process	1.84	2.04	9800
2: Plasma, healing process	1.08	1.06	50
3: Plasma + wet, healing process	1.02	–	40
4: IBE, healing process	0.63	0.66	90

Measured bulk lifetimes, extracted bulk life-times, and extracted SRV for each sample are summarized in Table III. Figure 10 shows the inverse measured carrier lifetime as a function of the inverse photoconductor width for sample 1, in which a linear increase can be observed. Applying the model, we can extract a bulk lifetime of 2.04 μs, which is very close to the measured bulk lifetime of 1.84 μs. A SRV of 9800 cm/s can also be extracted from this fit. In his review, Lopes[27] reports SRV values from 100 cm/s to 10^6 cm/s depending on the minority-carrier lifetime measurement technique and on the model used to extract the SRV.

Figure 11a and b show the use of the model with the data from samples 2 and 4, respectively. Again, the extracted bulk lifetimes of 1.06 μs and 0.66 μs are very close to the measured values of 1.08 μs and 0.63 μs. The extracted SRVs are 50 cm/s and 90 cm/s, respectively. Firstly, compared with sample 1, these values are significantly reduced. This shows how effectively the post-etch healing process can reduce the sidewall recombination rate. This result can also be correlated to the conductivity measurements.
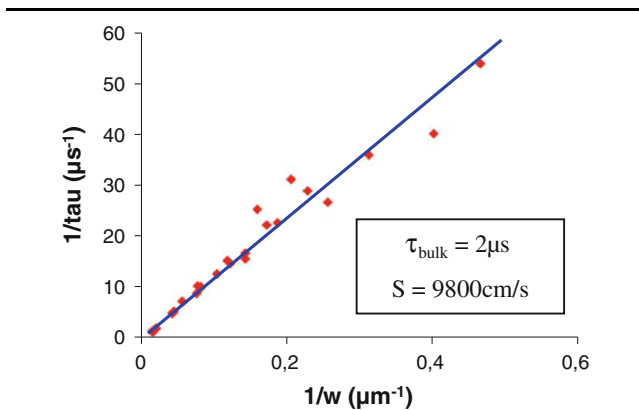
Minority carriers are more likely to interact with the depleted sidewalls of sample 1 than with the accumulated sidewalls of samples 2 and 4. Secondly, samples 2 and 4 exhibit different effective SRVs. This shows that different etching processes result in different electrical properties even after the post-etch healing process. This allows the study of different etching processes while using a standard photodiode process flow (that includes the post-etch healing). Finally, the ion-beam-etched sample has a larger effective SRV than the plasma-etched sample. However, it is difficult to conclude on the actual SRV of the ion-beam-etched sample due to the reduced shielding of the sidewalls with respect to the plasma-etched sample (Table II). Hence, this higher effective SRV value may arise from a greater number of induced sidewall recombination sites and/or greater interaction of minority carriers with these sites.

Sample 3 displays different behavior (Fig. 12a). Firstly, the measured carrier lifetimes are greater than the measured bulk lifetime (1.02 μs for this sample), which was not the case for the previous three samples. To explain this, we need to take into account that the measured bulk lifetime is the result of bulk recombinations as well as top and back surface contributions. To explain the behavior observed in Fig. 12a, a partial shielding of the top surface must be considered, which expands underneath the top surface from the sidewall toward the bulk as illustrated in Fig. 12b(1). This partial shielding of the top surface is supposed to be independent from the previously described sidewall shielding resulting from carrier accumulation. The cause of this partial shielding of the top surface is not fully understood. As the photoconductor width decreases, the top surface contribution is reduced [Fig. 12b(2)], and the measured lifetimes tend to increase compared with the measured bulk lifetime, approaching the real bulk lifetime. For a narrower photoconductor, the top surface is completely shielded [Fig. 12b(3)]. From that point, any lifetime variation is due to sidewall

Fig. 10. Inverse measured lifetime as a function of inverse photoconductor width for sample 1.
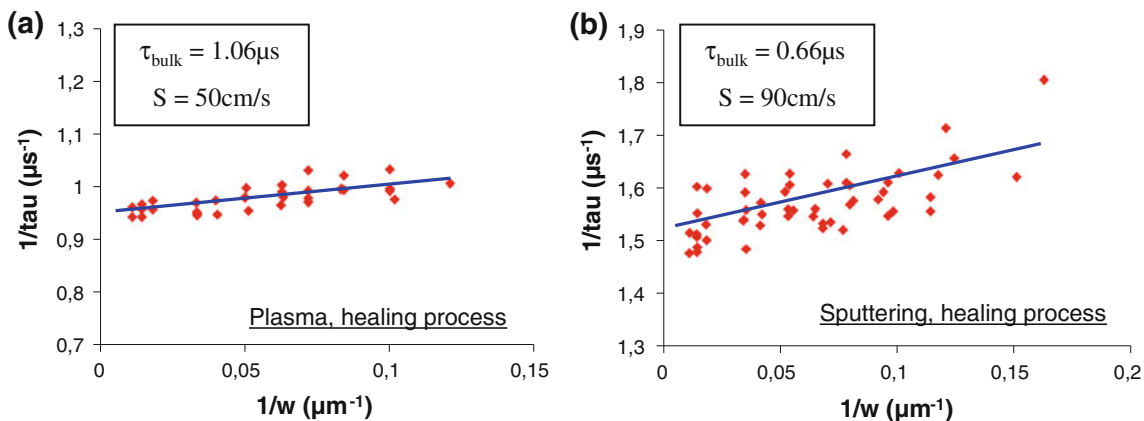

Fig. 11. Inverse measured lifetime as a function of inverse photoconductor width for samples 2 (a) and 4 (b).
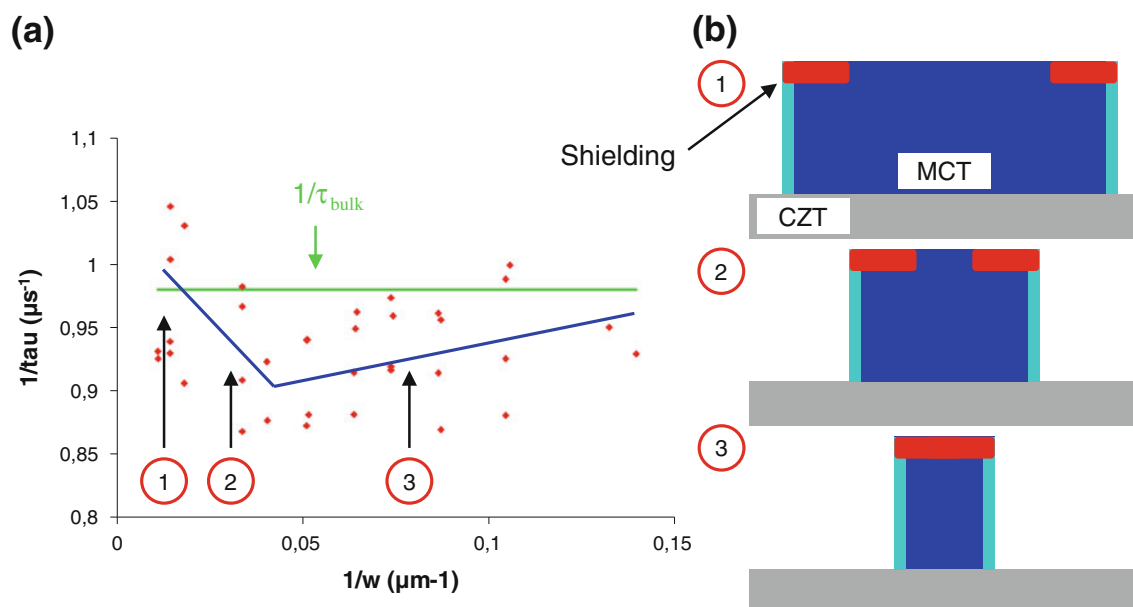
Fig. 12. (a) Inverse measured lifetime as a function of inverse photoconductor width for sample 3. (b) Schematic diagram of photoconductor cross-section for different widths.

recombinations. Applying our model to this part of the graph [Fig. 12b(3)], it is possible to extract an effective SRV of 40 cm/s. Comparison of the extracted and measured bulk lifetimes is irrelevant for this sample because the top surface contribution does not affect the lifetime of the photoconductors, whereas measurements on planar patterns include a top surface contribution. This effective SRV is slightly lower than the effective SRV value of 50 cm/s of sample 2. However, direct comparison of these two samples is difficult. Given the scatter of the dataset, a difference of 10 cm/s between the two SRV values is almost indistinguishable from the error. Also, the origin of the shielding effect of the top surface is unknown. However, within the framework of our present interpretation, this result indicates that the actual SRV is lower for sample 3 than for sample 2. Taking into account the conductivity measurements (Table II), we know that the sidewall shielding effect is much weaker for sample 3 than for sample 2. However, the extracted effective SRV values are similar for the two samples, indicating a strong reduction of the actual SRV for the hybrid plasma + wet etched sample compared with the plasma-etched sample. Additional experiments must be undertaken to understand the origin of the top surface shielding observed in the hybrid plasma + wet etching sample.

CONCLUSIONS

The effect of three different etching types on HgCdTe sidewalls was examined using AES and conductivity/minority-carrier lifetime measurements. No stoichiometric evolution was detectable with Auger analysis, which means that the potential microstructural damage induced by etching is lower than the demonstrated X_{Cd} discrimination limit, $\Delta X_{Cd} = 0.02$. Conductivity measurements show that plasma etching without an appropriate post-etch healing process leads to either carrier depletion or reduced mobility on the photoconductor etched faces. These measurements also showed that, after a post-etch healing process, samples displayed either carrier accumulation or enhanced mobility on their etched faces. Among the healed samples, IBE seemed to induce less conductivity changes than plasma etching. However, a light wet etch following plasma etching greatly restricted the plasma-induced conductivity change. Minority-carrier lifetime measurements showed that the post-etch healing process reduces the effective SRV of the etched sidewalls by several orders of magnitude. This effective SRV is expected to be a result of the combination of the actual SRV and a sidewall shielding effect that is due to band bending at the semiconductor surface. The study of the effective SRV values shows that IBE alters more profoundly the electrical characteristics than plasma etching, and that the hybrid plasma + wet etched sample presents a reduced actual SRV compared with the plasma-etched sample.

Conductivity and minority-carrier lifetime measurements were used to study etching methods for infrared detector fabrication. The effects of plasma etching, plasma + wet etching, and IBE were distinguished. In the future, other etching processes will be characterized, such as other plasma etching

recipes and IBE + wet etching. These studies, carried out on dedicated test structures, will also be correlated with measurements on actual photodiodes fabricated adjacent to etched trenches.

REFERENCES

1. A. Rogalski, *Rep. Prog. Phys.* 68, 2267 (2005).
2. A. Rogalski, *J. Appl. Phys.* 105, 091101 (2009).
3. V. Srivastav, R. Pal, and H.P. Vyas, *Opto-Electron. Rev.* 13, 197 (2005).
4. J.T.M. Wotherspoon, U.K. Patent No. GB2095898 (1981).
5. M.V. Blackman, D.E. Charlton, M.D. Jenner, D.R. Purdy, J.T.M. Wotherspoon, C.T. Elliott, and A.M. White, *Electron. Lett.* 23, 978 (1987).
6. E. Belas, J. Franc, A. Toth, P. Moravec, R. Grill, H. Sitter, and P. Höschl, *Semicond. Sci. Technol.* 11, 1116 (1996).
7. J.M. Baker, M.D. Jenner, J.M. Parsons, R.A. Ballingall, I.D. Blenkinshop, and J.H. Firkins, *IEEE Conf. Publ.* 228, 12 (1983).
8. G. Bahir and E. Finkman, *J. Vac. Sci. Technol. A* 7, 348 (1989).
9. J.M. Dell, J. Antoszewski, M.H. Rais, C. Musca, J.K. White, B.D. Nener, and L. Faraone, *J. Electron. Mater.* 29, 841 (2000).
10. B.A. Park, C.A. Musca, J. Antoszewski, J.M. Dell, and L. Faraone, *J. Electron. Mater.* 36, 913 (2007).
11. M. Seelmann-Eggebert and H.J. Richter, *J. Vac. Sci. Technol. A* 6, 2699 (1988).
12. H.M. Nitz, O. Ganschow, u Kaiser, l Wiedmann, and A. Benninghoven, *Surf. Sci.* 104, 365 (1981).
13. D.R. Rhiger and R.E. Kvaas, *J. Vac. Sci. Technol.* 21, 168 (1982).
14. R. Kiran, R. Sporken, T.N. Casselman, P.Y. Emelie, R. Kodama, Y. Chang, F. Aqariden, S. Velicu, J. Zhao, and S. Sivananthan, *J. Electron. Mater.* 37, 1471 (2008).
15. S. Mallick, R. Kiran, S. Ghosh, S. Velicu, and S. Sivananthan, *J. Electron. Mater.* 36, 993 (2007).
16. R.R. Singh, D. Kaushik, M. Sharma, D.K. Gupta, and R.K. Pandey, *Semicond. Sci. Technol.* 23, 015016 (2008).
17. R. Sporken, R. Kiran, T. Casselman, F. Aqariden, S. Velicu, Y. Chang, and S. Sivananthan, *J. Electron. Mater.* 38, 1781 (2009).
18. A.J. Stoltz, J.D. Benson, and P.J. Smith, *J. Electron. Mater.* 37, 1225 (2008).
19. F. Boulard, J. Baylet, and C. Cardinaud, *J. Vac. Sci. Technol. A* 27, 855 (2009).
20. E.P.G. Smith, C.A. Musca, D.A. Redfern, J.M. Dell, and L. Faraone, *J. Electron. Mater.* 29, 853 (2000).
21. J. Baylet, O. Gravrand, E. Lafosse, C. Vergnaud, S. Ballerand, B. Aventurier, J.C. Deplanche, P. Ballet, P. Castelein, J.P. Chamonal, A. Million, and G. Destefanis, *J. Electron. Mater.* 33, 690 (2004).
22. W. Yin, W. Zhou, and J. Huang, *Proc. SPIE* 7658, 4A (2010).
23. I.G. Gale, J.B. Clegg, P. Capper, C.D. Maxey, P. Mackett, and E. O'Keefe, *Adv. Mater. Opt. Electron.* 5, 79 (1995).
24. E.H. Cirlin, P. Ireland, S. Buckingham, and O. Wu, *J. Vac. Sci. Technol. A* 6, 2631 (1988).
25. C.K. Shih, D.J. Friedman, K.A. Bertness, I. Lindau, and W.E. Spicer, *J. Vac. Sci. Technol. A* 4, 1997 (1986).
26. M.A. Kinch, F. Aqariden, D. Chandra, P.-K. Liao, H.F. Schaake, and H.D. Shih, *J. Electron. Mater.* 34, 880 (2005).
27. V.C. Lopes, A.J. Syllaios, and M.C. Chen, *Semicond. Sci. Technol.* 8, 824 (1993).